Simulation-based assessment of railhead repair welding process parameters

Citation for the original published paper (version of record):

Andersson, B., Steyn, E., Ekh, M. et al (2025). Simulation-based assessment of railhead repair welding process parameters. Welding in the World, Le Soudage Dans Le Monde, 69(1): 177-197.
http://dx.doi.org/10.1007/s40194-024-01837-y

Welding in the World (2025) 69:177–197
https://doi.org/10.1007/s40194-024-01837-y

RESEARCH PAPER

Simulation-based assessment of railhead repair welding process parameters

Björn Andersson[1] · Erika Steyn[1] · Magnus Ekh[1] · Lennart Josefson[1]

Received: 1 March 2024 / Accepted: 10 September 2024 / Published online: 27 September 2024

Abstract
This study uses a finite element method based simulation methodology for in-situ railhead repair welding to investigate how welding process parameters impact the repaired rail quality. The methodology includes material modeling with cyclic plasticity, phase transformations, transformation-induced plasticity, and multi-phase homogenization. The weld process modeling includes a 3D heat transfer analysis and a 2D Generalized Plane Strain (GPS) mechanical analysis. The Heat source model used in the thermal simulation is calibrated using measurements from a repair welding experiment. To assess the performance of the repaired rail, mechanical rolling contact simulations are performed to estimate the risk of fatigue crack initiation. The process parameter study is based on the Swedish stick-welding railhead repair procedure and focuses on factors affecting the repair quality, such as preheating and operation temperature conditions as well as variations in repair geometry. Significant findings highlight both the inherent robustness of the process and regions susceptible to parameter variations. Specifically, the powerful final zig-zag weld passes provide effective resilience against variations in additional heating, and the start and end stretches of the repair welding are the most susceptible to parameter variations. Chamfered and deeper cutout repair geometries are found to be effective in mitigating adverse effects. In agreement with field observations, the simulations identify the fusion zone of the base and weld filler material as the critical region of the repaired rail in operation. This is attributed to the integrated effects of unfavorable microstructures, longitudinal tensile residual stresses from repair welding, and tensile stresses during operational traffic loads.

Keywords Welding simulation · Railhead defect repair · Numerical simulations · Phase transformation · Residual stress · Over-rolling simulation

1 Introduction

In today's railway networks, with intensified traffic, higher speeds, and increased axle loads [1–3], rail surface wear and damage are inevitable challenges. To meet these challenges, effective rail maintenance is essential for minimizing interruptions in railway operations [4], with repair welding playing an important role in restoring the rail surface quality in events of local damage [5]. Repair welding offers a cost-efficient and more sustainable alternative to replacing entire rail sections [6–8]. However, in terms of mechanical analysis it has not yet been investigated to the same extent as welding techniques for joining rail, such as flash butt welding, see, e.g., [9–11], or aluminothermic (thermite) welding, see, e.g., [12–14]. This knowledge gap underscores the significance of the detailed investigations into the process parameters governing of railhead repair welding presented in this study.

Several aspects of the mechanics at play in railway wheel-rail contact are uniquely challenging due to both high contact pressures [15–17] and the high number of loading cycles [18–20], also due to extended timeframes and length scales, often spanning decades over stretches of thousands of kilometers. Consequences of maintenance decisions may, therefore, manifest long after actions are taken, making the task of

---

Recommended for publication by Commission XIII - Fatigue of Welded Components and Structures.

✉ Lennart Josefson
lejo@chalmers.se

[1] Department of Industrial and Materials Science, Chalmers University of Technology, Gothenburg, Sweden

improving rail maintenance incredibly complex [21–23]. In this context, continued investigation and improvement of the existent numerical simulations enable both anticipation and mitigation of potential rail surface damage before disastrous consequences occur.

Numerical simulations, particularly finite element analysis, have long been valuable tools for understanding the general welding process, enabling the prediction of residual stresses and the assessment of microstructural transformations [24–26]. The application of these tools has, of course, extended to many railway welding processes, providing important insights into the residual stress field [27–29]. Moreover, rail welding simulations often incorporate over-rolling simulations to evaluate the fatigue performance in welded rail sections [30–33], a matter of utmost importance considering that a significant proportion of rail fractures occur in the vicinity of welds [34–36]. In this study, we, therefore, extend the numerical tools for repair welding established in previous works [37–39] to also include over-rolling simulations and evaluation of fatigue crack initiation.

The research objective of the presented study is to investigate how railhead repair welding process parameters impact the quality of the repaired rail section. Hence, we present a systematic process parameter study that investigates key factors, including preheating conditions, the shape of the railhead cutout, and the choice of filler material. The novelty of this contribution compared to other railhead repair welding simulations in the literature, see, e.g., [40–42], is primarily the insight into how the different process parameters affect the quality of the repair and greater detail in several modelling aspects. These aspects include multi-phase homogenization, accounting for cyclic hardening plasticity, repair welding simulations using continuous addition of filler material, empirically based post-repair over-rolling simulations, and calibration of the weld torch heat-source. Moreover, this study is specifically adapted to the stick-welding railhead repair process employed in the Swedish railway system. This adaptation is accomplished by conducting a railhead repair welding experiment and subsequent calibration of the simulation model based on experimental measurements. The insights derived from this research have the potential to improve the quality and effectiveness of in-situ arc welding repairs on railheads, thereby contributing to improved railway maintenance practices.

1.1 Present study

The present study is structured as follows; Sect. 2 describes the in-situ railhead repair welding considered in this study, providing an overview of the processes and techniques involved. Section 3 presents the material modelling and simulation methodology employed, highlighting the approaches used to simulate the repair welding process. Section 4 addresses the critical issue of heat source modelling accuracy and presents a simple railhead repair welding experiment designed to tune and adjust the heat source model by comparing experimental measurements with phase transformation simulation results. In Section 5, the tuned model is used to simulate a complete railhead repair in accordance with The Swedish Transport Administration's regulations. Next, in Section 6, we conduct a systematic study of the welding process parameters and investigate how variations in these parameters affect the railhead repair. Finally, in Section 7, we evaluate the quality of the repaired rail by assessing its mechanical performance under over-rolling conditions using a multi-axial fatigue life assessment based on the Dang Van stress.

2 The in-situ railhead repair welding process

In railway infrastructure maintenance, one of several imperatives is to ensure the structural robustness and longevity of rail tracks. Discrete rail surfaces damage such as cracks, squats, wheel-burns or other structural issues that could compromise rail integrity can be cost-efficiently repaired using the in-situ railhead repair welding process [6–8], as presented in the current study. In accordance with the Swedish regulations for stick-welding railhead repairs [43–45] (and also European equivalent [46]), damaged sections of the railhead are identified and removed, typically employing milling or cutting techniques, to eliminate all the damaged material as illustrated in Fig. 1. Importantly, the cut-out is done at a 45° angle with respect to both the vertical and axial direction.

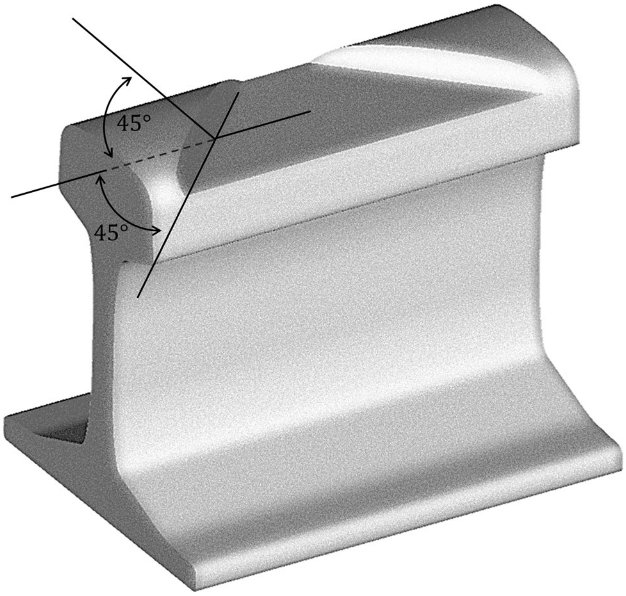

Fig. 1 Illustration of railhead repair cutout, highlighting the cutout angles

The next step, prior to filling the cut-out gap with new material, involves proper preparation for the welding process. The preparation involves detaching adjacent sleepers and raising the rail to facilitate access to the repair area, ensuring a clear path for the welding process. Moreover, to minimize the effects of intense temperature gradients during the welding process, a propane torch is used to preheat the rail to a specified preheating temperature of 350°C. The preheated area includes the cutout section to be repaired and also extends 100 mm to either side of the cutout. Next, skilled welders execute the repair weld with precision, adhering to established welding procedures and verification protocols. The welding procedures include longitudinal weld passes along the outer edges of the rail to build support ridges for the succeeding higher power, zig-zag weld passes deposited in between the outer support ridges. The chemical composition of the weld filler material (ESAB OK Wartrode 30 [47, 48]) and the R260 rail steel considered in this study is presented in Table 1. To ensure optimal weld operating conditions, the propane torch is used to reheat the rail cutout section to the preheating temperature limit if the temperature falls below the specified operating threshold of 300°C during the welding procedure, before proceeding with the next weld passes. Following welding, grinding is employed to remove excess surface material and restore the railhead geometry. Finally, a quality inspection is carried out to assess the weld's integrity and identify any surface or subsurface defects or irregularities that may compromise rail safety [49]. This inspection consists of non destructive testing; visual inspections and, based on the weather conditions at the day of the repair, ultra-sonic testing to identify potential subsurface porosities.

3 Simulation methodology

This chapter presents the constitutive material model, the simulation methodology of the repair welding and over-rolling simulations, and the FE-models used in the simulations.

3.1 Material model

Railhead repairs using arc welding subject the material to multiple local heating cycles and the material will therefore undergo multiple phase transformations. The temperature-driven transformations considered are listed below. Note that pearlite, bainite, and tempered martensite are referred to as phases even though they are in fact microstructures:

1. Pearlite into austenite during heating
2. Austenite into martensite during high cooling rates
3. Austenite into pearlite and/or ferrite during cooling
4. Austenite into bainite for moderate cooling rates
5. Tempering of martensite and bainite during heating
6. Martensite into austenite during heating
7. Bainite into austenite during heating
8. Melting and solidification

The modelling of the kinetics of the phase transformations 1 to 8 and how they occur during the cyclic heating in multi-pass welding is described in detail in previous works [37–39] and will here only be summarized briefly. The diffusive transformations upon heating, (1,6 and 7) and upon cooling (3 and 4) are modelled using the Johnson-Mehl-Avrami-Kolmogorov (JMAK) equation [51, 52]. Which describes the decreasing volume fraction for a constant temperature. Varying temperatures is handled using Scheil's additive rule [53, 54]. The displacive transformation of austinite into martensite during rapid cooling is modelled by using the purely temperature-dependent Koistinen-Marburger equation [55]. Melting and solidification phase transformations are modeled by linear development of a liquid-like phase. Note that temperature limits for melting and solidification are set to temperature levels below the physical melting temperature, 1200°C and 1500°C, respectively. Whereby the simulated liquid-like phase serves as a mechanical simulation cut-off at high temperatures. Finally, the material data used in the study, i.e., continuous cooling temperature diagrams and austenitization diagrams, is obtained from JmatPro [56].

To achieve a physically realistic behavior during the multi-phase stages of the welding process, it is necessary for a softer phase to be capable of undergoing plastic deformation while a stiffer phase simultaneously exhibits elastic behavior. We obtain this constitutive behavior using a self-consistent homogenization method [38] where the constitutive models of the individual phases are run in parallel. This method employs an analytically based, incremental strain-driven algorithm [57]. In each time increment, both the global

Table 1 Chemical composition of R260 rail steel [50] and weld filler material ESAB OK30 Weartrode [48]

	C	Mn	Si	P	Mo	S	Cr	Al	V	Fe
R260	060−0.82	0.65−1.25	0.16−0.60	≤0.03	≤ 0.08	≤0.03	≤0.15	≤0.004	≤0.03	bal.
Weartrode	0.1	0.7	0.7	–	–	–	3.2	–	–	bal.

strain increment and temperature are given, with temperature assumed to be uniform across all phases. Material states from the previous time increment, along with homogenized strain and stress, are also considered as given inputs. Using this data, the homogenization framework calculates strain increments of each individual phase, using a fourth-order concentration tensor. This tensor is computed using the global algorithmic stiffness tensor, each phase's individual algorithmic stiffness tensor, and the Eshelby tensor through a fixed-point iteration scheme [58, 59]. Based on the strain increments of the individual phases, their respective stresses and stiffness tensors are computed and the overall homogenized stress and stiffness tensor for the current time increment is determined again using the volume fractions and concentration tensors.

The constitutive model used for each phase can be described, in short, by its small strain additive decomposition of the total strain. The total strain is assumed to be constructed by six strain components; elastic, plastic, thermal, transformation, transformation-induced plasticity (TRIP), and discretized annealing. The elastic strain governs the stress, and we assume linear isotropic elasticity by applying Hooke's law. For the plastic strain of each phase, we employ a Chaboche plasticity model, as proposed in, e.g., [60], including the von Mises yield function, non-linear isotropic and kinematic hardening. Thermal expansion and transformation strains are considered isotropic due to volume changes during heating and phase transformations. The latter is determined by phase densities and the conservation of mass. TRIP strain arises from phase transformation under applied stress, with the underlying physics described in, e.g., [61–63]. We allow for TRIP during the transformation of austenite into martensite or bainite, adopting the formulation proposed by LeBlond [64, 65]. The importance of capturing virgin state recovery during melting and solidification is well documented, see, e.g., [66]. Therefore, we reset the plastic strains, hardening, and load history effects using a numerically discretized annealing strain component to ensure that the material solidifies into a stress-free virgin material state.

During the railhead repair considered in this study, a single material point may repeatedly undergo several of the listed phase transformations. This is due to the multi-pass, multi-layer welding process inherent in the repair process, which subjects the material point to multiple heat cycles, for which the cooling rates can vary significantly. We have demonstrated this effect, and transient development of stresses during welding for a simplified welding example (plate butt welding) in a previous work [39].

3.2 Repair welding simulation

We employ a computationally efficient simulation methodology presented in a previous work [39]. In essence, this methodology decouples the thermo-mechanical finite element analysis into a transient thermal analysis and a quasi-static mechanical analysis. The temperature field obtained from the thermal analysis is used as input for the mechanical analysis, in which the temperature field drives metallurgical processes and thermal expansions, which, in conjunction with mechanical loading, governs the mechanical response.

The thermal analysis entails a 3D, full-scale simulation of the repair weld process, incorporating a moving double ellipsoid heat source, as described by Goldak et al. [67, 68], to represent the specific heat flux input. The heat source is presented in the following equation and is implemented in Abaqus [69] by a user-defined subroutine:

$$q(x, y, z) = \frac{6\sqrt{3} f_i Q_0}{abc\pi\sqrt{\pi}} e^{-3\left((x/a)^2+(y/b)^2+(z/c_i)^2\right)} \tag{1}$$

The power Q_0 and traversing speed of the heat source are adjusted to match the measured values from the experimental welding procedure, with the power computed based on current and voltage ($Q_0 = VI$). The dimension parameters of the heat source, a, b, and c, are fine-tuned to ensure that the area of the simulated phase-transformed regions correlates with experimental measurements. Moreover, the heat input front and rear fractions f_i are set to $f_i = f_f = 0.6$ for the front section and $f_i = f_r = 1.4$ for the trailing section. During the simulation, filler material is continuously added using the quiet element approach [70–72]. This method activates individual filler elements as the moving heat source passes the element.

Compared to the thermal analysis, the mechanical analysis typically involves higher computational costs. However, by adopting the aforementioned simulation methodology [39], we circumvent this issue. In this methodology, the mechanical analysis utilizes a 2D Generalized Plane Strain (GPS) model of the rail cross-section, using Abaqus' CPEG elements [69], which assumes that the 2D cross-section has constant curvature with respect to the out-of-plane, axial direction and lies between two rigid bounding planes. Moreover, the modelling is extended to account for the rail's out-of-plane axial and bending stiffnesses. The stiffnesses, assigned to the bounding planes, are verified by beam theory and allow for precise modelling of the out-of-plane stress component. Specifically, for the cross-section under consideration, our methodology has demonstrated the ability to replicate results obtained from the more computationally intensive 3D model [39], while also aligning closely with repair welding residual stress measurements [42]. Additionally, the simulation methodology has been further verified by comparing it with surface residual stress measurements on laser-heated railway steel samples [73].

3.3 Over-rolling simulation

Post-repair over-rolling simulations are carried out to study the mechanical performance of the repaired rail section using the crack initiation criterion of Dang Van to estimate the multiaxial fatigue initiation limit. The over-rolling simulation setup uses parts of the multi-step over-rolling simulation methodology presented in [74], called over-rolling methodology in the following.

The over-rolling methodology was originally designed to predict the long-term degradation of rail profiles in crossings due to mixed traffic conditions, taking into account various factors like contact forces, wear, and plastic deformations. In short, the methodology consists of a set of iterative and multidisciplinary simulations and analyses; full-scale dynamic vehicle-track interaction simulations using field measurement load sequences, involving multiple vehicles and repetitions, provide contact load inputs for subsequent FE simulations. The FE simulations are carried out in 2D, where the transition from 3D to 2D is accomplished by adjusting the 2D model to preserve the maximum von Mises stress of the 3D contact simulations. The 3D contact results are obtained from a metamodel [75] that is trained against 3D normal contact FE-simulation results. Lastly, predictions of accumulated plastic deformation and wear from the 2D simulations are used to update the dynamic vehicle-track interaction simulation before each new iteration.

We use one iteration of the over-rolling methodology, starting from field measurements to deriving the 2D equivalent over-rolling loading sequence. To elaborate, for the conversion of quasi-static 3D contact loads to the 2D GPD model is done by scaling the boundary load per unit length of the 2D model individually to match the maximum von Mises stress of the 2D over-rolling simulation to the 3D over-rolling simulation. The scaling factors are computed a-priori and implemented through the force equilibrium in the element assembly of the FE-solver. Furthermore, the load sequence is based on 483 wheel passage field measurements from a curved rail section along the Western mainline in Sweden, between Nyckelsjön and Sparreholm, and consists 90% passenger trains with axle loads varying from 11.7 to 21.0 tonnes, and 10% freight trains with 22.5 tonnes axle load [76]. The sequence is repeated several times to generate multiple thousands of over-rolling wheel passages. In contrast to the over-rolling methodology, this repetition is done without regenerating the load sequence. Therefore, the effect of possible wear and contact position variations in successive load sequences is not accounted for. Lastly, it should be noted that the curved rail section considered is especially suited for the 2D GPD model implementation as only transverse traction loads can be accounted for in the simulations. The transverse traction load applied varies between 5 and 10% of the normal load.

The effect of repair welding residual stress redistribution during over-rolling operational loads is estimated using the Dang Van stress fatigue criterion [77]. This multiaxial fatigue criterion is used to assess the risk of fatigue crack initiation in materials subjected to complex stress conditions in elastic shakedown conditions. The probability of crack initiation due to material slip bands and opening of existing micro-cracks is estimated based on the hydrostatic stress and the shear stress “amplitude” (the deviation from the mid-value during a stress cycle) on a critical shear plane. Conveniently, the criterion does not rely on a predetermined critical shear plane but instead examines the fulfillment of the criterion for all possible shear planes. Therefore, it has a reputable history of use in fatigue analysis of railway welding applications [41, 78, 79], particularly in situations of rotating principal stresses and multiaxial stresses. During the time of a full-load cycle, fatigue crack initiation is expected if the following inequality is fulfilled:

$$\sigma_{\mathrm{eq,DV}}(t) = \tau_{\mathrm{Tr,a}}(t) + \langle c_{\mathrm{DV}}\sigma_{\mathrm{h}}(t)\rangle > \tau_{\mathrm{e}} \tag{2}$$

where σ_{h} is the hydrostatic stress, c_{DV} a non-dimensional material constant ($c_{\mathrm{DV}} = 1/3$ REF), $\langle\bullet\rangle$ Macaulay brackets, and $\tau_{\mathrm{Tr,a}}$ the Tresca shear stress “amplitude” computed using the maximum and minimum principal stresses of the deviatoric stress tensor “amplitude,” $\sigma_{\mathrm{dev,a,I}}$ and $\sigma_{\mathrm{dev,a,III}}$:

$$\tau_{\mathrm{Tr,a}}(t) = \frac{1}{2}\left(\sigma_{\mathrm{dev,a,I}} - \sigma_{\mathrm{dev,a,III}}\right) \tag{3}$$

3.4 FE-model of rail geometry

The FE-models used for the simulations are based on a rail of European rail profile 60E1 [50]. Figures 2 and 3 present the 3D model used in the heat transfer analysis and the 2D GPD models [39] used in the mechanical analysis. Three cross-sections are considered in the study; cross-section 1 through the center of the repaired rail section, cross-section 2 through the chamfered section, and cross-section 3 through the start of the cut-out. It is important to note that, despite the 2D assumption being less accurate in cross-sections 2 and 3, a simple comparison of 2D and 3D mechanical response (in simulations without phase transformations) shows how local effects and general trends are captured, with reasonably good agreement. In the 3D model, the mesh of the weld layers and HAZ in the regions adjacent to the 2D cross-sections considered in the mechanical analysis has a characteristic element length of approximately 0.25 mm. Whereas in the far field regions, both in the cross-section and in the axial direction, the mesh gets gradually coarser to minimize computational cost. For the 2D GPD models, the mesh has the same characteristic element length of approximately 0.25 mm for the weld layers and HAZ, and a gradually coarser mesh for the

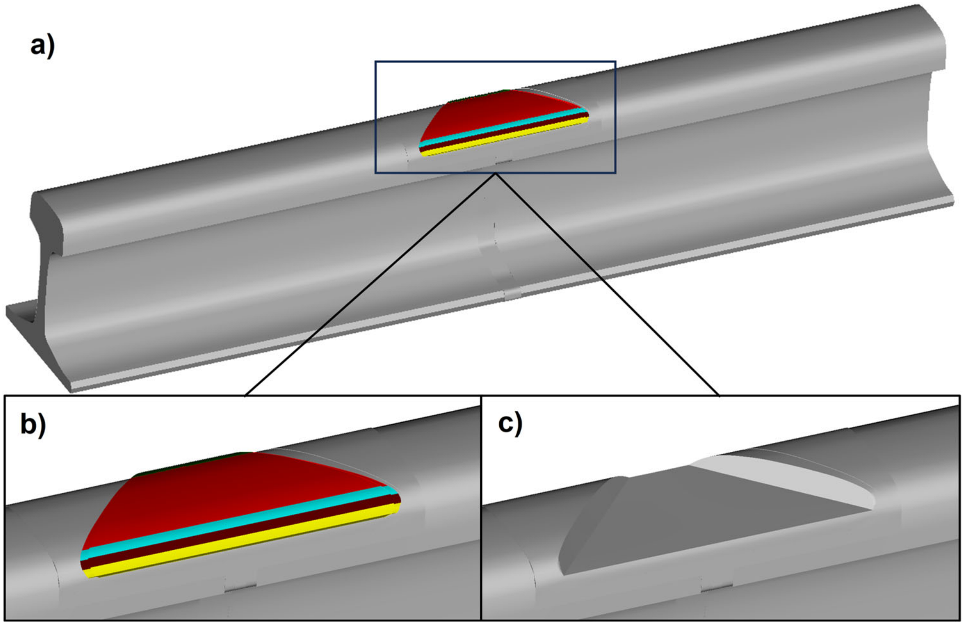

Fig. 2 **a** 3D FE-model used in the heat transfer analysis, **b** railhead repair highlight, and **c** railhead damaged section cut-out highlight. The distinctive colors represents the different longitudinal and zig-zag weld passes

far field regions in the rail web and rail foot. An important consideration in determining the chosen element length is the necessity to resolve temperature gradients to a degree such that resulting regions with local phase transformations span multiple elements.

Figure 2c illustrates the cutout of the railhead which is to be repaired, in accordance with the Swedish regulatory railhead stick weld repair procedure as outlined in Sect. 2. The cutout has a depth of 10 mm, measures 40 mm at the shorter edge and 180 mm at the longer edge. The distinctive colors in Fig. 3b correspond to individual weld passes, with five longitudinal passes at each edge to create the outer ridges and two zig-zag passes to fill the gap between the ridges. The longitudinal weld passes start at cross-section 3 and move in the direction toward cross-section 1, whereas the final zig-zag weld passes start in the opposite end. Note that the top layers include 2 mm of excess filler material which is removed by correcting grinding after the repair process. However, the simulations do not model the full effect of this grinding explicitly but remove these elements using the quiet element approach. Therefore, possible heating effects during grinding are not accounted for, only stress redistributions due to element removal.

When simulating the experimental procedure to calibrate the welding heat source, the FE model is set-up to replicate the experiment using simple image correlation. 2D coordinates are extracted from images of the repaired rail and used to reproduce the overall shape of the added weld material in

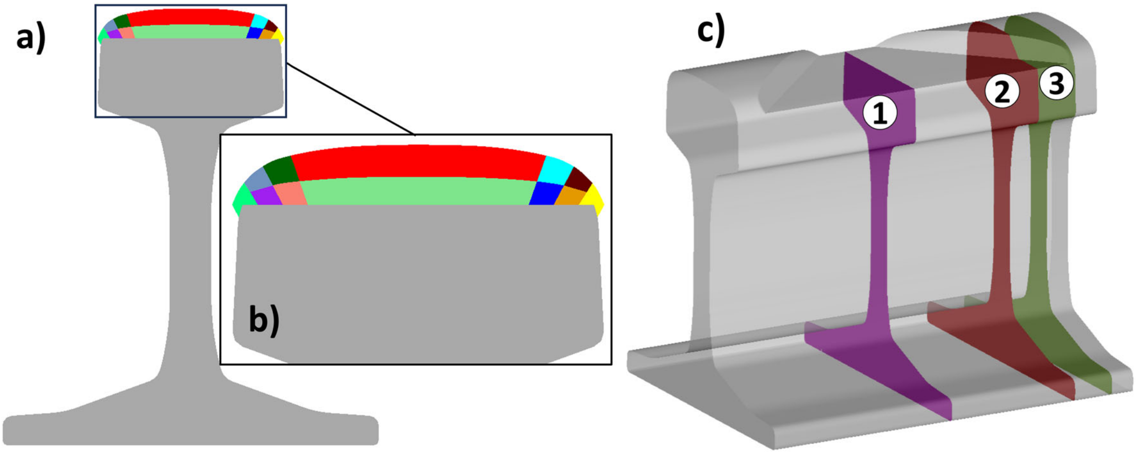

Fig. 3 **a** 2D FE-model used in the heat transfer analysis, **b** railhead repair highlight, and **c** the three cross sections investigated in 2D mechanical analyses. In **a** and **b**, the distinctive colors represent the different longitudinal and zig-zag weld passes of the two weld layers

the FE model. For the 3D model, this shape is extracted in the axial direction to construct the repaired section of the rail.

The simulations of the experimental procedure and the complete railhead repair welding use the same boundary conditions; In the thermal analyses, radiation and convective boundary conditions are applied to the surface of the rail. While in the mechanical analyses, only the master node of the 2D GPD model's element formulation is constrained in the weld simulations and the bottom nodes of the rail foot during the over-rolling simulations.

4 Railhead repair welding experiment

It is well known that in computational welding mechanics (CWM), the accuracy of the heat input modeling governs the fidelity of the simulation outcome [80–82]. To address this issue, this chapter presents a simple railhead repair weld experiment, used to tune and adjust the heat source modeling by comparing experimental measurements and simulation results.

4.1 Experiment procedure

The experiment and its equivalent FE-model are illustrated in Fig. 4. Note that this is a simplified surface repair weld procedure used only for FE-model tuning and verification purposes. For example, no damaged material is removed, and the repair welding is performed at the edge of the rail specimen and not at the center. However, the experiment is otherwise carried out in accordance with the Swedish regulatory railhead stick weld repair procedure outlined in Sect. 2, including thorough surface preparation, preheating of the specimen, and operating temperature monitoring. The weld procedure consists of a series of 16 weld passes; 15 vertically stacked, longitudinal weld passes to the rail corner, followed by a final zig-zag weld pass on the horizontal, top surface, covering half of its width. These weld passes are illustrated by different colors in Fig. 4d. Specific parameters for each weld pass, such as current, voltage, and traversing speed, were recorded and are presented in Table 2. The recorded values align with recommendations found in literature, e.g., [83]. Moreover, it should be mentioned that the experiment bares significant resemblances to the repair procedure of a worn, or damaged, railway switch frog.

Throughout the welding procedure, the surface temperature was monitored with a laser thermometer. To maintain the desired operating temperature, reheating was performed at the end of every fifth weld pass. Once the welding procedure was completed, the specimen was left to cool naturally, without the application of any forced cooling.

4.2 FE-simulation

The experimental procedure was replicated in an simulation using the FE model illustrated in Fig. 4. The basic aspects of the FE model setup have been presented in Sect. 3.4. In the simulation of the experimental procedure, the preheating process was implemented by applying a surface heat flux of 60 kW/m^2 to the preheated surface for a duration of 500 s. For the succeeding weld passes, the power and traversing speed of the moving heat source were set to match the values recorded during the experiment, see in Table 2. These parameters are considered as fixed inputs in the heat source calibration. Whereas the dimensional parameters of the heat source were manually fine-tuned to ensure the simulation accurately produced phases transformed regions consistent with the hardness measurements provided in Sect. 4.4. The final heat source dimensional parameter values, i.e., a, b, $c_i = c_f$ and $c_i = c_r$ in Eq. 1, were set such that its width ($2a$) and depth (b) correspond to the width and height of the weld bead, and its front and trailing extent to 1/2 and 3/4 of the bead width. The heat source starting point in each weld pass was set at the end of the rail specimen and at the center of each

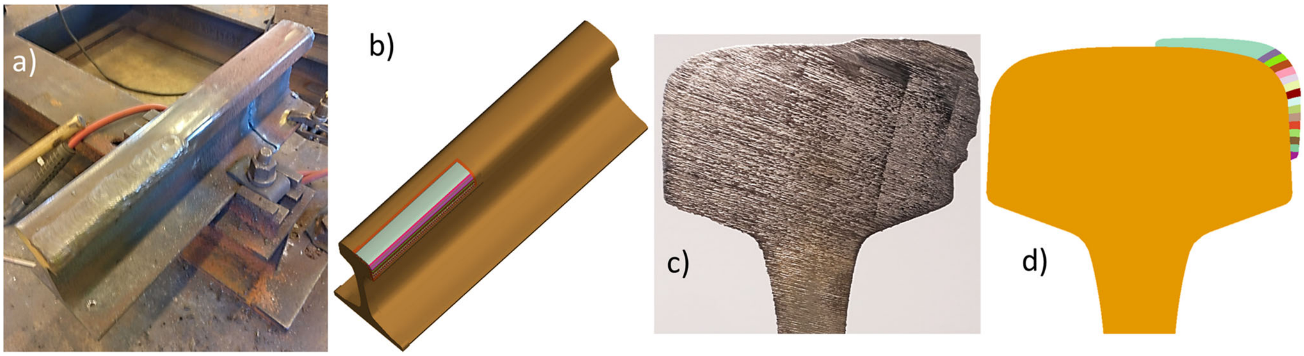

Fig. 4 **a** experimental rail surface repair welding setup, **b** FE-model of experimental setup, **c** cross-section of repaired rail, and **d** FE-model of cross-section with different colors illustrating the 16 weld passes. The total length of the rail is 660 mm while the length of repaired section is 220 mm

Table 2 Welding process parameters during rail surface repair process

Weld pass	1	2	3	4	5	6	7	8	9	10	11	12	13	14	15	16
Time [s]	20	22	28	32	35	44	48	53	49	55	56	49	53	58	44	247
Current [A]	166	166	166	166	166	166	166	166	166	166	166	166	166	166	166	210
Voltage [V]	29	29	29	29	29	25	25	25	25	25	25	25	25	25	25	25
Speed [mm/s]	11.0	10.0	7.9	6.9	6.3	5.0	4.6	4.2	4.5	4.0	3.9	4.5	4.2	3.8	5.0	4.4

weld bead cross-section. Importantly, the heat source double ellipsoid was rotated such that its vertical axis is aligned with the direction of the rail surface normal for each weld pass. The rotation of the heat source can be interpreted as the weld stick being orthogonal to the surface. Furthermore, the heat input efficiency was set to 80% for the phase transformations of the experiment and simulation correlate. This value agrees with high-efficiency arc welding power sources as suggested by, e.g., [84].

Acknowledging the practical need to reposition the weld torch and remove slag between each successive weld pass, a 30 s wait was introduced between each weld pass as well as before and after the reheating procedures. The reheating was simulated identically to the preheating method but was applied for a duration of one minute, to attain the specified preheating temperature of 350 °C and thus ensuring that a satisfactory operating temperature is maintained. The final top surface weld layer was simulated by 47 transverse zig-zag weld passes. Furthermore, the simulation accounted for the effects of natural surface convection and surface radiation. The final cooling step of the simulation was terminated once the simulation reached a steady-state condition.

4.3 Measurement procedure and equipment

In order to assess the mechanical properties and the microstructure of the repair-welded railhead, a series of experimental measurements were conducted. Vickers hardness (HV) indentation measurements were performed on the entire cross-sectional surface of the railhead. These measurements were carried out using a 1 kg indentation weight in a Struers Emcotest DuraScan 70 G5 hardness tester. Samples for microscopy were prepared by mechanically polishing with a diamond solution and then etched with a 3% Nital solution (HNO3 in ethanol). The prepared samples were examined using a Zeiss Axioscope 7 microscope with Zen Core 2.7 software.

4.4 Experimental measurements and simulation results

Figure 5a and b present the results from the indentation hardness measurements of the repair-welded railhead and micrograph images highlighting the HAZ, respectively. From the results, the outline of the HAZ can clearly be identified by the texture transition highlighted in Fig. 5b and by the significant increase in hardness and, suggesting that the microstructure has undergone phase transformations. Similar hardness values are presented by Popovic et al. [85] for bainitic microstructure resulting from railhead repair welding. Moreover, Fig. 5a also illustrates the three calibration paths used to compare the experimental results and the sim-

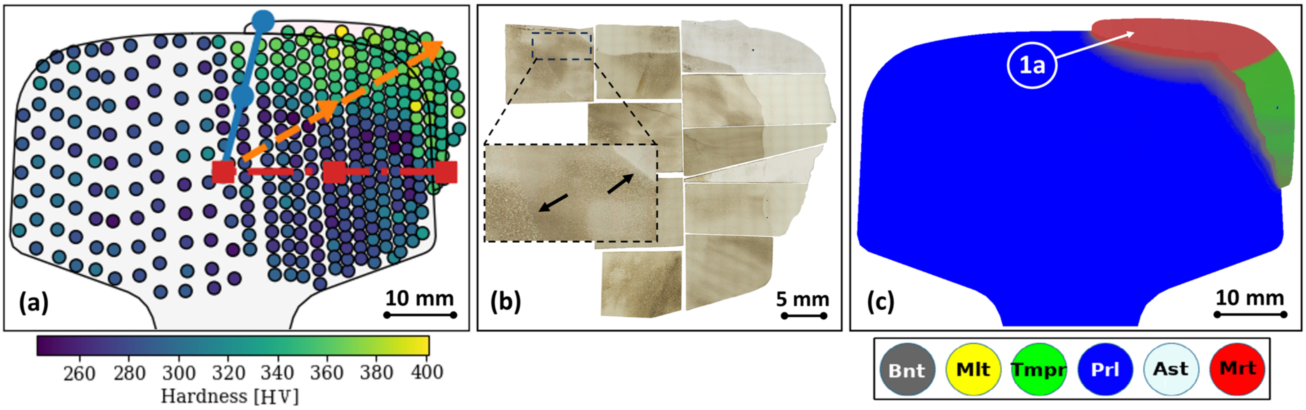

Fig. 5 **a** hardness measurements [HV] and illustration of paths used for FE-model heat source calibrations. **b** micrograph images highlighting the HAZ of the repaired rail corner. **c** simulation results of the rail surface repair welding experiment material phases

ulation results. The hardness results along these paths are plotted in Fig. 6, where volume fraction simulation results are also presented.

In Fig. 6, the HAZ is easily distinguishable due to deviations from the initial state of the material in terms of both hardness and phase volume fractions. The nominal hardness of the pearlitic R260 rail material is 260 HV. Within the HAZ, the measurements indicate an increase in hardness and the simulation results predict a multi-phase microstructure. Furthermore, Fig. 6 demonstrates a good correlation between the simulation and experimental results regarding the size of the areas that have undergone phase transformations. This indicates a satisfactory calibration of the heat source.

The FE-simulation of the welding experiment gives the final fields of the material phases as shown in Fig. 5c. The color scheme used to illustrate the material phases primarily shows which phase that is dominating. For instance, the predicted phase fractions at highlight 1a are approximately 7/10 martensite, 1/5 retained austenite, and 1/10 bainite. More detailed information about the phase fractions along the calibration paths is given in Fig. 6.

5 Repair welding — regulatory procedure

5.1 FE-simulation set-up

The Swedish railhead stick weld repair procedure, approved by the Swedish Transport Administration as outlined in Sect. 2, is simulated using the FE-model presented in Sect. 3 and the welding heat source established in Sect. 4. Specifically, the initial longitudinal weld passes, which create supporting ridges for the final zig-zag weld passes, are simulated using the welding process parameters of the first 3 weld passes of the experimental procedure, as shown in Table 2. The final zig-zag passes, used to fill the gap between the ridges, are simulated similarly to the top surface weld pass in the experiment, i.e., using the parameters of weld pass 16 in Table 2.

5.2 Simulation results

Figure 7 presents simulation results from the reference case in three columns and two rows. Each column corresponds

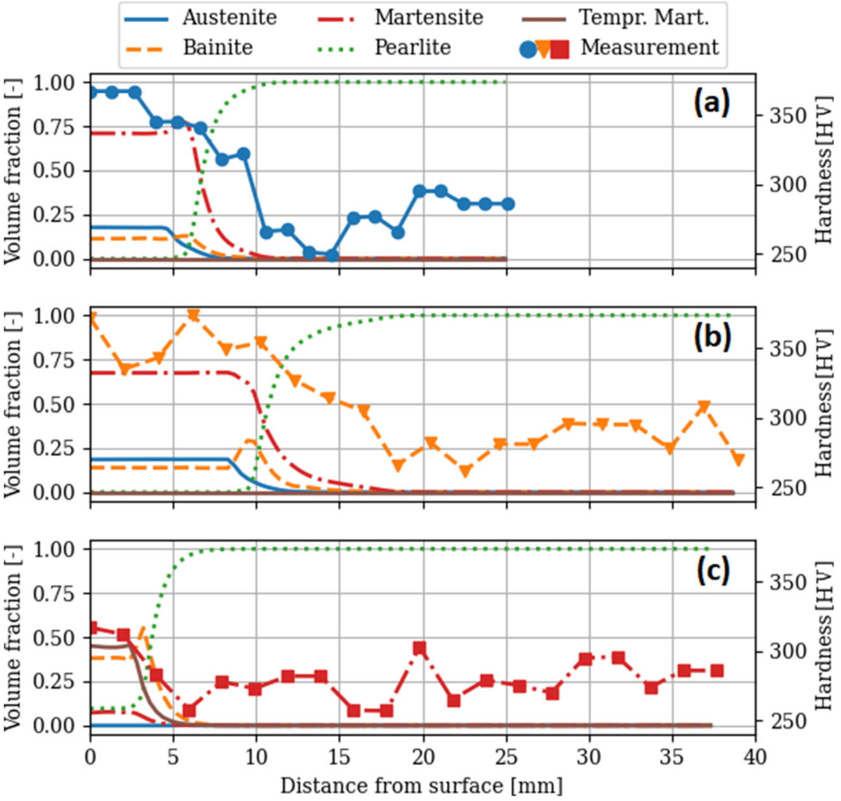

Fig. 6 Hardness measurements [HV] and simulated volume fractions [-] plotted along the calibration paths defined in Fig. 5a: **a** along red square-marked line, **b** along orange triangle-marked line, and **c** along blue circle-marked line

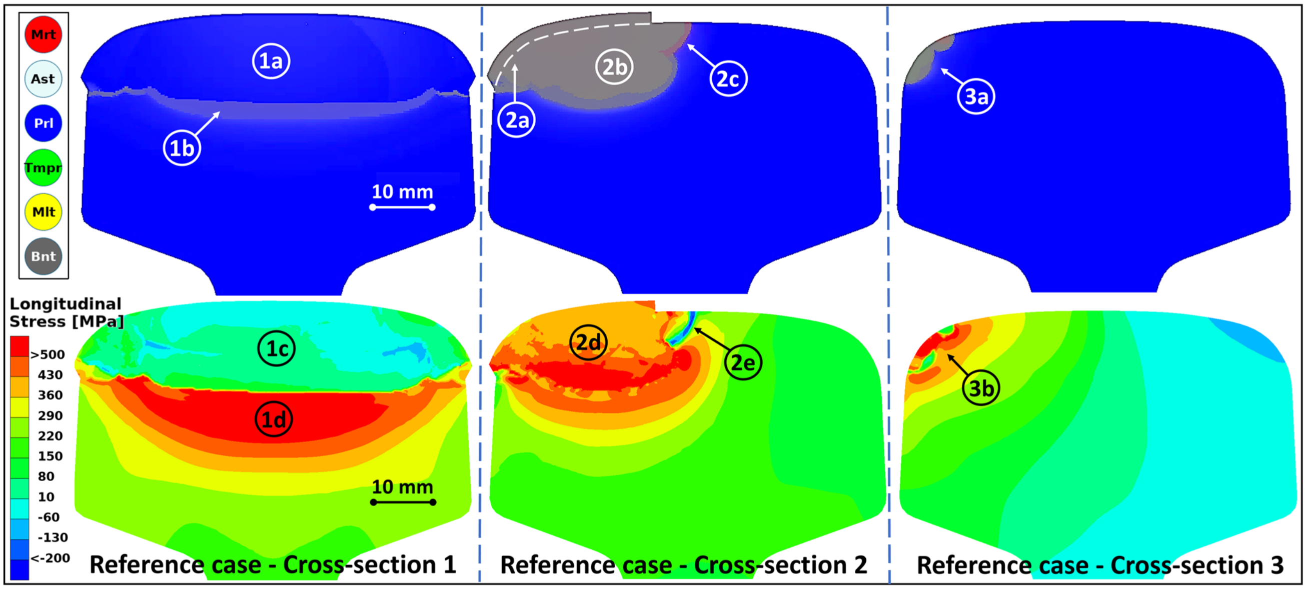

Fig. 7 Reference case simulation results. First row: phase volume fraction illustrations; red, martensite; white, austenite; blue, pearlite; green, tempered martensite and/or bainite; yellow, melt; and grey, bainite. Second row: longitudinal residual stress fields. First column: cross-section 1. Second column: cross-section 2. Third column: cross-section 3. Highlights are explained in the Section 5.2

to one of the 2D cross-sections defined in Fig. 3c. The first row provides rudimentary illustrations of the phases obtained after the repair welding, while the second row presents the longitudinal stress component of the residual stress field. Investigating these results, it is evident that for cross-section 1, the substantial heat input from the zig-zag weld passes results in slow cooling rates, facilitating pearlite formation in both the filler material and melted base material (highlight 1a). Consequently, the residual stress in this region is relatively low (highlight 1c). However, it should be noted that by using the weld filler material presented in Table 1, the resulting microstructure (highlight 1a) is not a fully pearlitic microstructure. The lower carbon content produces a ferritic-pearlitic microstructure. For illustrative simplicity, this is not presented in Fig. 7, moreover, it is also deemed to have minor effects for the presented residual stress state. Moreover, in the adjacent HAZ (highlight 1b) of the R260 base material, the predicted material phase is a mix of pearlite and bainite, adding to the tensile residual stresses in this region (highlight 1d). The general profile of the maximum longitudinal residual tensile stresses occurring some distance beneath the surface aligns with experimental [42] and numerical [41] findings in the literature.

Furthermore, the chamfer of the cutout leads to shorter zig-zag weld passes at the start and end stretches of the repair rail compared to the full rail width of cross-section 1. As cross-section 2, see Fig. 3c, cuts through the chamfered section only half of the cross-section will be subjected to repair welding, visible by the excess filler material (highlight 1a). This results in less heat input and faster cooling rates, resulting in a fully bainitic microstructure (highlight 2b) and tensile residual stresses (highlight 2d). Additionally, it also results in a small band with some martensite content (highlight 2c) which consequently produces compressive stresses (highlight 2e). The width of the martensic band is 1 mm, which with the fine mesh resolution constitutes 4 elements in width.

In the case of cross-section 3, the material does not reach melting temperatures; however, the austenization temperature is reached in the uppermost corner of the rail cross-section. This region then experiences cooling rates rapid enough for bainitic transformations (highlighted in 3a). The heating and phase transformations of this region cause tensile residual stresses (highlight 3b). Note that the phase transformations occur during initial, longitudinal support ridge weld passes and not during the zig-zag weld passes.

The distinct stress gradients, evident in all residual stress plots presented in Fig. 7, e.g., between highlights 1c and 1d, can be partially attributed to the mechanical properties of the filler material applied to all previously molten material. Whereas, the primary contributor to these gradients is the annealing discretization effect resulting from the simulated virgin material state during solidification, as described in Sect. 3.1. This modeling results in a significant difference in material hardening and thermal contraction for the molten and unmolten regions. Considering the stress gradients, it is important to note that the presented stress fields utilize the nodal average of stresses calculated at adjacent integration points, providing a continuous and smoothed stress representation.

When comparing repair welding to thermite or flash butt rail welds, the difference in thermal load profiles produces notably different residual stress states within the rail. For the repair welding process, the asymmetric concentration of heat in the upper section of the rail causes stronger thermal contraction in the railhead compared to the rail web and rail foot, resulting in the residual stress state presented in Fig. 7. In contrast, thermite welding and flash butt welding uniformly subject the entire cross-section to thermal load, resulting in a more homogeneous thermal contraction. These procedures typically produce compressive stresses in the railhead and rail foot, counterbalanced by tensile stresses in the rail web, c.f. [9, 14]. Consequently, the mechanical performance of repair welding requires considerations in railway operation and maintenance. Reports and failure analyses of rail fractures in the field identify the interface between weld filler material and rail base material as particularly critical for fatigue crack initiation [86]. As an example, Fig. 8 shows a fractured rail where beach marks indicate that the fatigue crack was initiated in the fusion zone of the shallow rail surface repair weld (highlight 1). The fusion zone being the critical region can also be identified from the results presented in Fig. 7, in terms of concentrations of both tensile residual stresses and more brittle material phases.

6 Repair welding — process parameter study

6.1 Preliminaries

The quality of in-situ welded railhead repairs is believed to be significantly influenced by temperature gradients throughout the welding procedure, which are dictated by the overall temperature distribution during the repair process. The preheating temperature limit, the minimum allowed operating temperature, and repair geometry are the primary factors influencing the temperature distribution in the repair welding process. Therefore, to demonstrate the value of numerical simulation tools in enhancing railhead repair welding procedures, this study presents a process parameter study with two primary focuses: variations in preheating and in-process reheating conditions, and variations in the geometry of the repair. Additionally, a change of weld filler material is also taken into consideration.

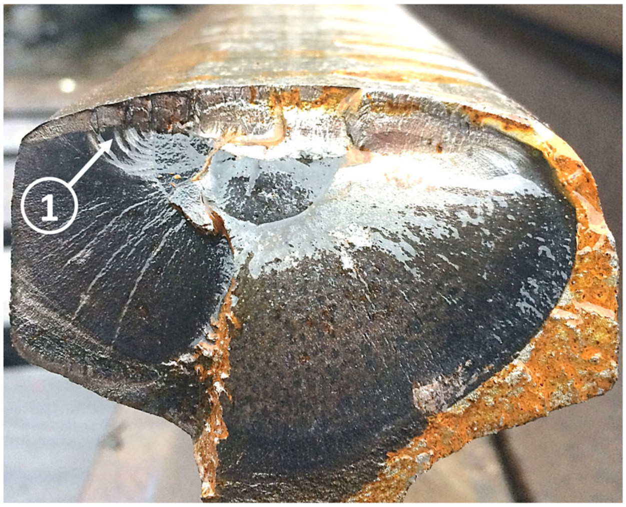

Fig. 8 Fractured rail with a shallow surface repair weld. Highlight 1 roughly indicates the surface repair weld [86]

Motivating our primary focuses, firstly, the operating temperature is crucial due to its susceptibility to unintended variations caused by operator errors or changing of weather conditions. In addition, there is a necessity to investigate the relationship between regulatory temperature limits for pre- and reheating and the temperature intervals for phase transformations of the material, particularly the martensite starting temperature. Secondly, variations in repair geometry affect both the total heat input and its distribution during the repair process and are consequently important for the repaired rail's quality. While the geometry of the repair is dictated by welding specifications and is likely less susceptible to unintended variations, this study explores variations to assess sensitivity to geometry variations and potential improvements. While welding parameters such as voltage, current, and torch directions are important, this study treats them as fixed due to their inherent stability against unintended variations.

Furthermore, the mechanical and metallurgical properties of the filler material used in the repair process will have a significant effect on the resulting phase transformations and final mechanical performance of the repaired rail. To illustrate this, an additional simulation is performed using the base material, i.e., R260 rail steel, as the simulated filler material.

Finally, to assess the mechanical implications of variations in pre- and reheating, as well as in cut-out geometry, we use the simulation of on the regulatory repair welding procedure, presented in Sect. 5, as a reference. This allows for the identification of the effects of alterations to the parameters of the repair welding process. As will be discussed in the following sections, only the most critical of the three cross-sections will be considered in the parameter study.

6.2 Process parameter variations

Four variations in pre- and reheating temperature limits are examined, as outlined in Table 3. The table presents the considered initial rail temperatures and the temperature limits. The presented cases span a range of scenarios, starting with case 1, a simulation using no pre- or reheating. For case 2, the temperature limits for pre- and reheating are increased by 100°C. Next, case 3 represents a worst-case scenario in accordance with governing regulations. This scenario considers the minimum allowable ambient rail temperature of -10°C and the maximum permissible measurement equipment error of ±5°C. Lastly, case 4 includes a postheating step, identi-

Table 3 Temperature limits for pre- and postheating and environmental temperatures considered in the repair welding simulations

Case	Temperature limits [°C] Rail	 Preheat	 Reheat	 Postheat
Ref.	20	350	300	*none*
1	20	*none*	*none*	*none*
2	20	450	400	*none*
3	−15	350	300	*none*
4	20	350	300	350

cal to the preheating procedure, after the final zig-zag weld passes are completed.

Table 4 presents the three variations of the geometry of the railhead repair weld considered in this study, where unmentioned aspects remain unchanged. The first, case 5, involves a more shallow 5 mm cut-out, resulting in a single layer repair weld. The second, case 6, considers a rectangular cutout (i.e., 90° cutout angles in Fig. 1) with a depth of 10 mm and a length of 100 mm. The third geometry variation, case 7, involves a (chamfered) cutout, 100 mm longer than the reference case. For case 8, the metallurgical properties of the filler material are set to match those of the R260 rail base material. It is important to note that this case, while perhaps less realistic, is investigated solely to explore the effect of the choice of weld filler material.

6.2.1 Heating variation simulations

Examining the simulation results for cross-section 1 in cases 1 to 4 reveals a noteworthy finding: the different surface heating conditions have minimal impact on the resulting phase transformations. For this cross-section, the heat input from the zig-zag weld passes is consistently sufficient for generating slow cooling rates and a fully pearlitic material. This insensitivity to pre- and postheating conditions suggests a reassuring robustness of this repair welding procedure. The same insensitivity and robustness were observed for cross-section 3. However, in contrast, for cross-section 2 the results are affected by different surface heating conditions. Similar results were obtained by [40], where high preheating gave negligible effect on final cooling rates, and a martensitic-bainitic microstructure was observed at the start and end stretches of the repair welding. The following discussion will, therefore, focus on cross-section 2, for which the results are shown in Fig. 9.

Table 4 Repair geometry and weld filler material variations considered in the repair welding simulations

Case	Geometry variations [mm] Cut out depth	 Cut out length	Filler material
Ref	10	35 / 175	Weartrode
5	5	35 / 175	Weartrode
6	10	100 (*no chamfers*)	Weartrode
7	10	135 / 275	Weartrode
8	10	35 / 175	R260

The first column of Fig. 9 presents case 1, where pre- and reheating were disregarded. This resulted in a predicted multi-phase state of approximately 1/5 martensite and 4/5 bainite (highlight 1a), with the lower martensite density leading to compressive residual stresses (highlight 1d). The simulation also revealed that omitting preheating led to martensite transformations for initial support ridge weld passes, subsequently tempered by the more powerful, subsequent zig-zag weld passes (highlight 1c and 1f). As in the reference case, a small band with martensite content (highlight 1b) with associated compressive stresses (highlight 1e) is obtained. This small band of martensite persists in varying degrees for all heating variations (highlights 2b, 3b, 4b, 2d, 3d, and 4d).

The results from case 2, presented in the second column of Fig. 9, demonstrate that elevating the operating temperature limits produced a fully bainitic material state (highlight 2a), similar to the reference case. Also, slower cooling rates and prolonged transformations in adjacent weld passes lead to slightly lower tensile stresses compared to the reference case and case 1 (highlight 2c).

The third column of Fig. 9 presents simulation results for the coldest allowable environmental conditions, case 3. These environmental conditions cause faster cooling rates; however, the prolonged phase transformations of the filler material still produce a fully bainitic material state (highlights 3a). Interestingly, the faster cooling rates produce lower tensile residual stresses at the rail surface (highlight 3c) and similar tensile stresses in the first zig-zag weld pass (highlight 3e).

Simulation results of case 4, where post-repair heating was applied, are presented in the fourth column of Fig. 9. Here, it is seen how the phases closely resemble the increased operating temperature case, case 2. In other words, a slower and more uniform cooling rate generates a fully bainitic material (highlight 4a). However, the tensile residual stresses become slightly higher in magnitude (highlight 4c), and the compressive stresses are slightly lower in the band with martensite content (highlight 4d). Finally, note that the critical region, in terms of both unfavorable microstructures and harmful stress states, for all four cases is located some distance beneath the rail surface.

6.2.2 Geometric variation simulations

The simulation results obtained for the repair geometry variations in cross-section 1 showed a minor impact on the

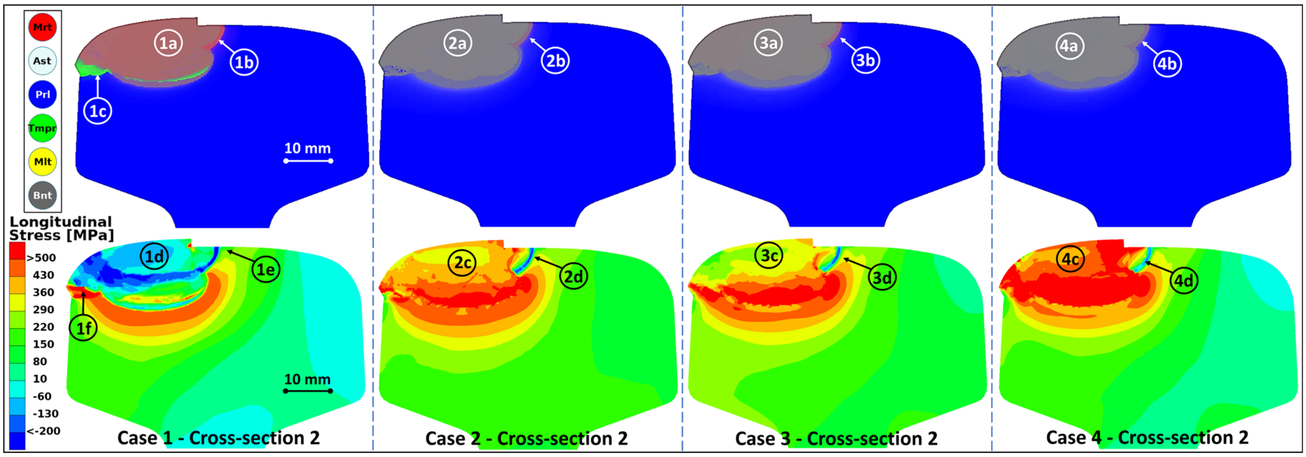

Fig. 9 Simulation results form cross-section 2. First row: phase volume fraction illustration; red, martensite; white, austenite; blue, pearlite; green, tempered martensite and/or bainite; yellow, melt; and grey, bainite. Second row: longitudinal residual stress field. First column: Case 1, no preheating. Second column: Case 2, higher operating temperature. Third column: Case 3, cold conditions. Forth column: Case 4, postheating. Highlights are explained in the Section 6.2.1

resulting phase transformations and residual stress. As for the pre- and post-heating variations for the same cross-section, the substantial heat input from the powerful zig-zag weld passes causes slow cooling rates, resulting in a fully pearlitic material for cases 5, 6, and 7. This robust trend was consistently observed in cross-section 3. In contrast, cross-section 2 exhibited greater sensitivity to changes in repair geometry by influencing the heat input and cooling rates and, consequently, affecting both phase transformations and residual stress states. Therefore, also the following discussions will focus on the results obtained for cross-section 2, illustrated by the simulation results presented in Fig. 10 with the cases 5 to 8 presented in separate columns.

The outcomes of case 5, simulating a shallower, 5 mm cutout, are presented in the first column. Here, the previously molten material obtains a multi-phase material state comprising approximately 1/10 martensite and 9/10 bainite (highlight 1a). Furthermore, the surrounding non-molten area exhibits a mix of approximately 3/10 martensite, 6/10 bainite, and 1/10 pearlite (highlight 1b), as a result of more rapid cooling rates. The lower density of martensite is evident by the compressive residual stresses (highlight 1d) and the tensile stresses of the previously molten material (highlight 1c).

The second column of Fig. 10 presents the results the rectangular railhead cutout simulation in case 6. The results presented show how similar to the chamfered railhead

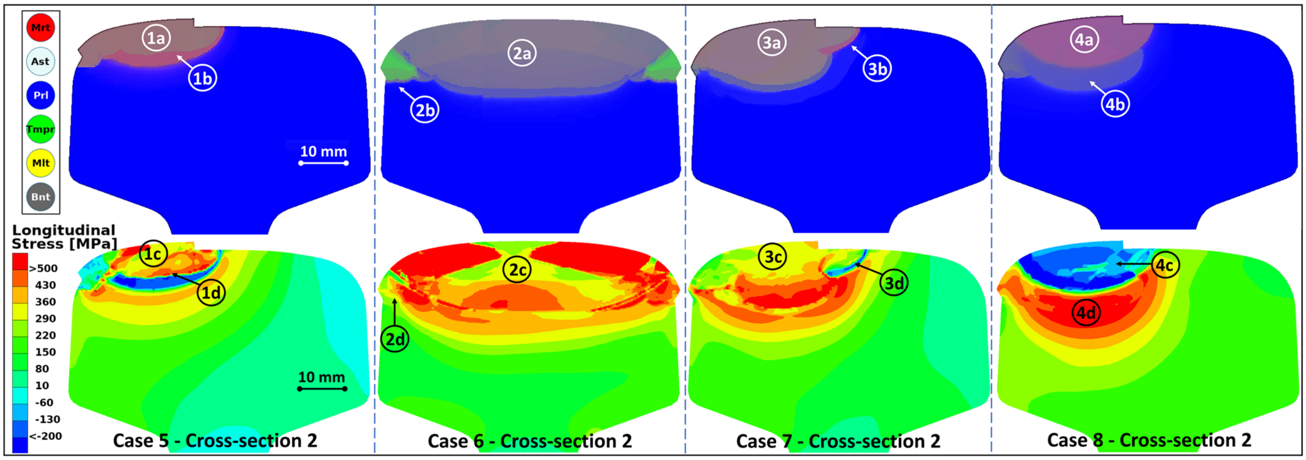

Fig. 10 Simulation results form cross-section 2. First row: phase volume fraction illustration; red, martensite; white, austenite; blue, pearlite; green, tempered martensite and/or bainite; yellow, melt; and grey, bainite. Second row: longitudinal residual stress field. First column: Case 5, shallow cut-out. Second column: Case 6, rectangular cutout (i.e., no chamfers). Third column: Case 7, longer rail repair. Fourth column: Case 8, R260 filler material. Highlights are explained in the Section 6.2.2

cutouts, this case produces a fully bainitic material (highlight 2a) at the start and end points of the repaired section of the rail. Moreover, the peculiar character of the residual stress field (highlight 2c) reveals information about cooling rates. Despite the entire repaired section consisting of the same phase, the outer corners of the final zig-zag weld pass exhibit significantly higher tensile stresses due to faster cooling rates. Furthermore, the initial longitudinal support ridge weld passes experience rapid cooling rates in this cross-section and produce a martensite which is tempered by subsequent zig-zag weld passes (highlight 2b). For these regions, the asymmetry of the zig-zag weld passes' heat input is believed to cause the asymmetric residual stress field (highlight 2d).

The third column of Fig. 10, corresponding to case 7 where the reference case cutout of the railhead is extended by 100 mm, demonstrates how longer weld passes allow for greater heat dissipation during the repair process and consequently more rapid cooling rates, resulting in outcomes similar to the colder environment in case 3. Specifically, a fully bainitic material (highlight 3a) and lower tensile stresses at the surface (highlight 3c). Also as seen in the heat variation cases, a small martensitic region due to the time-temperature history of the zig-zag weld passes (highlights 3b and 3d).

In the fourth column of Fig. 10, case 8 is presented, using R260 rail material metallurgical properties for the filler material. For this material, phase transformations occur significantly faster than for the Weartrode filler material. This results in a multi-phase material state of approximately 3/6 bainite, 2/6 pearlite, and 1/6 martensite for the second zig-zag weld pass (highlight 4a) and 2/3 bainite, 1/3 pearlite for the first zig-zag weld pass (highlight 4b). The resulting residual stresses differ significantly from those of the reference case, such that the use of R260 filler material induces stronger compressive stresses in the previously molten rail section (highlight 4c), and consequently higher tensile stresses in the surrounding region (highlight 4d). Finally, the critical region of the repaired rail section for the repair geometry variations is typically some distance below surface, although not as evident as for the heating variations.

The rail surface repair welding experiment presented in Sect. 4 can be considered as an additional case in the geometry variation study, in which material is added to the rail surface without the prior removal of damaged material. This process bears resemblance to a laser cladding process, as studied by, e.g., [87–89]. Consequently, Fig. 11 illustrates the residual stress field of the rail surface repair welding experiment. Highlight 1 in the figure illustrates the phenomenon of tensile residual stresses in the previously melted material. The material that has not undergone fusion in the region between the filler and the base material, as illustrated in highlight 2, is subjected to considerable compressive stresses. The HAZ, as illustrated in highlight 3, surrounding the region that has undergone phase transformations experiences a notable tensile residual stress. The aforementioned regions can be identified by the distinctive textures observed in Fig. 5b. A comparison of the material phases and residual stress fields in Figs. 5c, 11, and 10 Case 5 indicates that the rail is receiving less heat in the cladding-like process, particularly for the final zigzag weld pass. This results in higher cooling rates, a higher martensite content, as shown in Figs. 5b and c, and a distinct longitudinal residual stress state, as shown in Figs. 11 and 10 Case 5.

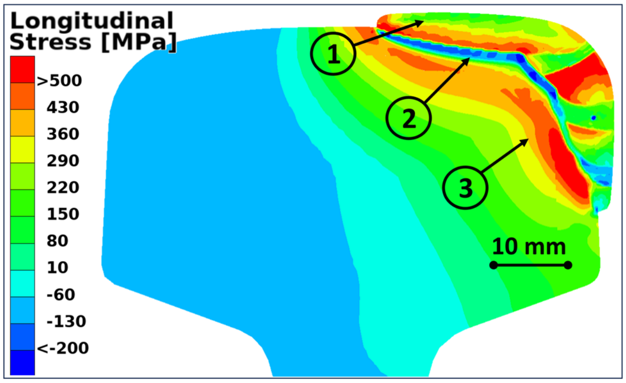

Fig. 11 Simulation results of the rail surface repair welding experiment: longitudinal residual stress. Highlights are explained in the Section 6.2.2

7 Repair welding — operational load performance

7.1 Roll-over simulations

The consequences of the repair welding residual stress fields on fatigue damage initiation during operational traffic loads are investigated in this subsection. Small differences in residual stress might lead to larger differences in fatigue life due to the cumulative nature of fatigue damage in high-cycle fatigue applications, such as the interaction between the rail and wheel, combined with the observed tensile repair welding residual stresses. To assess the influence on welding process parameters on fatigue life, simulations of 2000 train wheel over-rollings are conducted, as described in Sect. 3.3, for each repair welding case detailed in Tables 3 and 4. Subsequently, a fatigue crack initiation evaluation is performed where the Dang Van stress (see Eq. 2) is computed at five points below the rail surface on the gauge corner, illustrated in Fig. 12. Note that the wheel load passes over the long edge of the rail head repair.

7.1.1 Reference case

To provide a qualitative comparison of fatigue performance across the different repair welding cases, we introduce a baseline reference case where the over-rolling simulations are

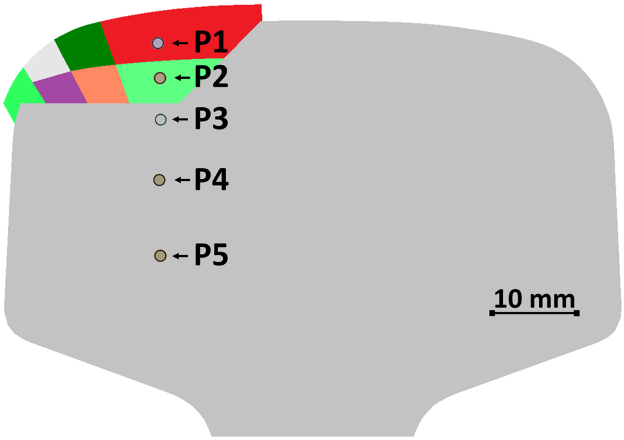

Fig. 12 Dang Van stress evaluation points for cross-section 2

performed using a non-repaired rail cross-section. In Fig. 13, the longitudinal residual stress component obtained after simulating over-rollings in the non-repaired cross-section is presented. These results show how over-rollings induce compressive residual stresses on the rail surface (highlights a, b, and c), balanced by tensile stresses deeper beneath the surface (highlight d). Furthermore, three main contact areas of the simulated wheel contact load spectrum can be clearly identified (highlights a, b, and c).

Figure 14 presents simulation results from the over-rolling simulations of the reference weld repair case. The figure illustrates the longitudinal stress component of the residual stress field for all three cross-sections after 2000 simulated over-rollings. When comparing the residual stress field produced by the repair welding (see Fig. 7) and the over-rollings on a non-repaired rail (see Fig. 13), these results demonstrate the expected outcomes. More specifically, they show how the welding residual stresses are somewhat redistributed, with strong compressive stresses superimposed on the rail surface (highlights 1a, 2a, 2b, 3a, and 3b) and tensile stresses

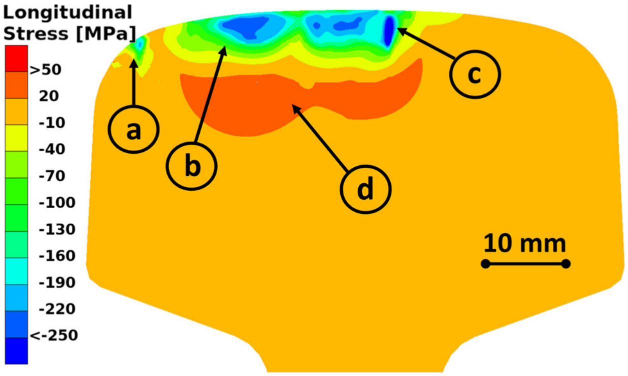

Fig. 13 Longitudinal residual stress after 2000 simulated over-rollings on a non-repaired material rail cross-section. Highlights a–c indicate compressive stresses at main contact patches and highlight d tensile residual stress regions

are slightly increased at a depth of 15 to 20 mm below the surface (highlights 1b and 2c).

7.1.2 Heating variation simulations

The following discussions will focus on cross-section 2, as it is the most sensitive to repair welding process parameter variations. Starting with the heating-related cases, Fig. 15 illustrates how the high surface pressure from the train wheels redistributes and alleviates the tensile welding residual stresses at the surface (highlights 1a–4a). Except for case 4, where strong tensile stresses persist in a small region (highlight 4c). This is explained by that this region is outside the wheel contact patch positions in the considered load collective illustrated in Fig. 13. Furthermore, similar to the reference case, cases 1 to 4 show consistency in the slight increase of tensile stresses beneath the surface (highlights 1b–4b).

7.1.3 Geometric variation simulations

Figure 16 presents the longitudinal residual stress fields after the over-rolling simulations for the geometry and filler material variations of the repair welding process. Similar to the results presented in Fig. 15, the over-rollings induce some compressive stresses at the rail surface (highlights 1a-4a) and show a minor effect on the subsurface stress states (highlights 1b–4b). Importantly, these results clearly illustrate both the persistence and the dominance of residual stresses from repair welding after simulated over-rollings. Particularly notable is case 6, where the tensile residual stresses at the rail surface (highlight 2a) are not redistributed or alleviated to the same extent as in the other parameter study cases.

7.2 Fatigue performance assessment

From the over-rolling simulations for the repair welding cases presented in Tables 3 and 4, the Dang Van stress is computed, for each over-rolling wheel passage, at the five points highlighted in Fig. 12. When assessing the computed Dang Van stresses, it is important to remember that an approximate 2D model has been adopted for the mechanical analyses and also that the over-rolling simulations do not account for bending or axial loads in the rail. Consequently, the Dang Van stress evaluation presented here is mainly focused on qualitative comparisons of the fatigue performance effects when varying repair welding process parameters. With this in consideration, the presented stresses are normalized by the maximum Dang Van stress from the non-repaired rail over-rolling simulation, i.e., that of Point 4.

In Fig. 17, the normalized maximum Dang Van stresses from all cases are presented, computed at each measuring point, see Fig. 12, in cross-section 2. Comparing these results

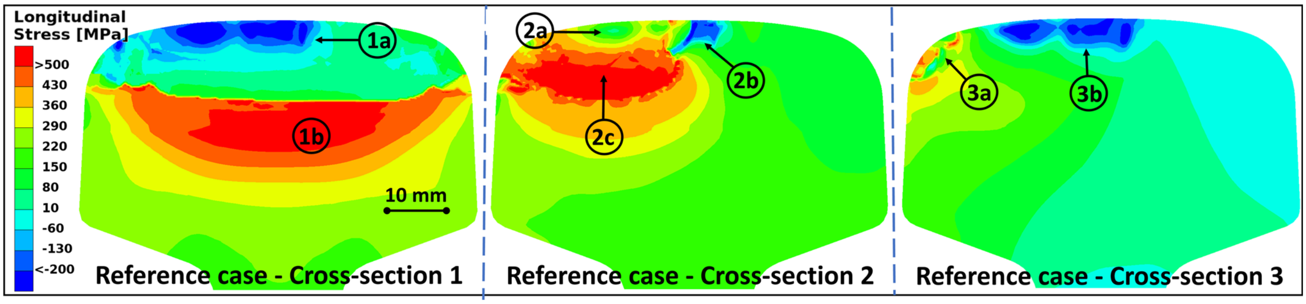

Fig. 14 Longitudinal residual stress from post-repair over-rolling simulations for the repair weld reference case. First column: cross-section 1. Second column: cross-section 2. Third column: cross-section 3. Highlights are explained in Section 7.1.1

to the non-repaired rail reference over-rolling simulation reveals that the Dang Van stress generally tends to increase in all measuring points. However, in point 3, which typically experiences the highest tensile residual stresses, for regions with the Dang Van stress decrease for most cases. This is due to that the stress state at this point is dominated by longitudinal residual stresses which are significantly larger than the stresses caused by over-rolling normal and transverse traction loads and thus cause a relatively low shear stress "amplitude," see Eq. 3.

Focusing on variations in process parameters related to heat input (cases 1 to 4) reveals that the post-heating in case 4, surprisingly, does not seem to achieve the intended improvement in the quality of the repair for the considered cross-section. Furthermore, for geometry and filler material variations, the longer repair (case 7) produces similar results as the reference case. Whereas the simulation using R260 weld filler material (case 8) appears to significantly elevate the Dang Van stresses close to the rail surface. Conversely, the shallower repair simulated in case 5 seems to decrease the Dang Van Stress closer to the rail surface. This is due to the lower heat input inducing lower overall residual stresses. However, this highlights a critical oversight in the fatigue performance comparison. Simply comparing the magnitudes of Dang Van stresses overlooks the crucial impact of phase transformations, particularly brittle phases. As highlighted in Fig. 10, case 5 produces a significant amount of martensite in the repaired section of the rail and does thereby not enhance the fatigue performance of the repaired rail, as indicated by Fig. 17.

In line with the simulations conducted for heating and geometric variations, the over-rolling simulations underscore the robustness of the existing repair welding process. However, the comprehensiveness of the roll-over simulations and fatigue crack initiation evaluation could be enhanced by incorporating additional loading components, such as rail bending and axial load, along with manufacturing residual stresses. Such extensions would add value to the Dang Van stress comparison of the simulation cases. Nonetheless, this refinement would most likely have minimal impact on the main conclusions of the subsurface region identified as critical and the repair welding procedure deemed fairly robust.

8 Conclusions and outlook

Numerical simulations have been used to investigate how the quality of repaired rail sections is affected by railhead repair welding process parameters. An experimentally validated thermo-metallurgical-mechanical finite element simulation methodology was used, including material models and weld process modeling [39, 73]. The material modeling accounts for kinematic and isotropic nonlinear material hardening, phase transformation kinetics, transformation-induced plas-

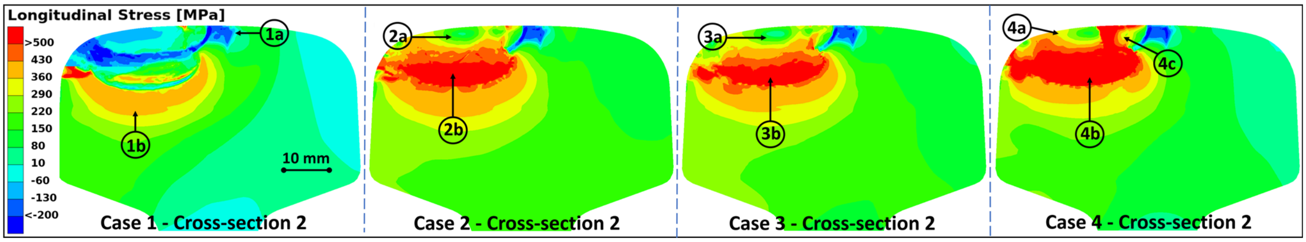

Fig. 15 Longitudinal residual stress field from post-repair over-rolling simulation for heat variation cases in cross-section 2. First column: Case 1, no preheating. Second column: Case 2, higher operating temperature. Third column: Case 3, cold conditions. Forth column: Case 4, postheating. Highlights are explained in Section 7.1.2

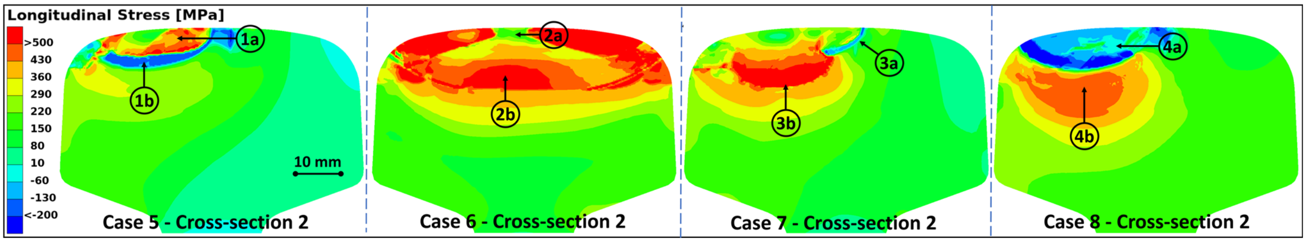

Fig. 16 Longitudinal residual stress field from post-repair over-rolling simulation for geometry variation cases in cross-section 2. First column: Case 5, shallow cut-out. Second column: Case 6, square cut-out (i.e., no chamfers). Third column: Case 7, longer rail repair. Fourth column: Case 8, R260 filler material. Highlights are explained in Section 7.1.3

ticity, and multi-phase homogenization. Furthermore, the welding process modeling includes a moving heat source and continuous addition of filler material. To ensure the fidelity of the welding simulation models, a simple repair weld experiment was conducted. By simulating this experimental procedure, the heat source model was tuned until a satisfactory correlation was achieved in terms of the simulated phase fractions and phase transformations indicated by hardness measurements. The tuned heat source model was used in a process parameter study of railhead repair welding, based on the Swedish regulatory procedure for railhead stick-welding repairs.

The primary focus of the parameter study was to analyze results from different preheating and operational temperature conditions, as well as variations in repair geometry. These process parameters in the repair welding procedure have the most substantial impact on the overall temperature distribution, spatial gradient, and time history. This governs the material response in terms of phase fractions, stresses, and strains, and consequently, the quality of the repair. It is also crucial to anticipate how the quality of the repaired rail might be affected by unintended variations arising from operator errors and unpredictable weather conditions. Furthermore, to assess the quality of the repaired rail sections in service, the repair welding simulations were extended to investigate the effect of operational traffic loads. This involved simulating the rolling action of train wheels on the repaired rail surface and assessing the mechanical fatigue performance of the repaired rail by comparing the Dang Van stress to that of a non-repaired rail.

The major findings of the parameter study are listed below.

- The powerful final zig-zag weld passes, providing the majority of the added material, generate significantly more heat than the propane torch used in pre-, re-, and postheating. Hence, the robustness of the procedure in terms of its insensitivity to variations in applied heating.
- Critical regions for process parameter variations are identified at the start and end stretches of repair-welded sections. To mitigate their negative impact on the rail performance, the shorter edge of the trapezoid-shaped rail repair should be oriented toward the gauge corner of the rail that is subjected to the most critical contact loading.
- In agreement with field observations, the simulations identify the fusion zone of the base material and weld filler material as the critical region of the repaired rail. This is attributed to the integrated effects of unfavorable material phases, longitudinal tensile weld residual stresses, and tensile stresses during operational traffic loads.
- Tensile residual stresses after welding at the rail surface tend to be redistributed and alleviated by train wheel passages. In contrast, residual stresses some distance below the rail surface exceed over-rolling residual stresses by

Fig. 17 Over-rolling simulation fatigue crack initiation evaluation; maximum Dang Van stress of five evaluation points (Fig. 12), in cross-section 2 (Fig. 3c) for all welding repair welding cases (Tables 3 and 4) normalized using the maximum Dang Van stress of Point 4 for the non-repaired (N-R) over-rolling reference simulation

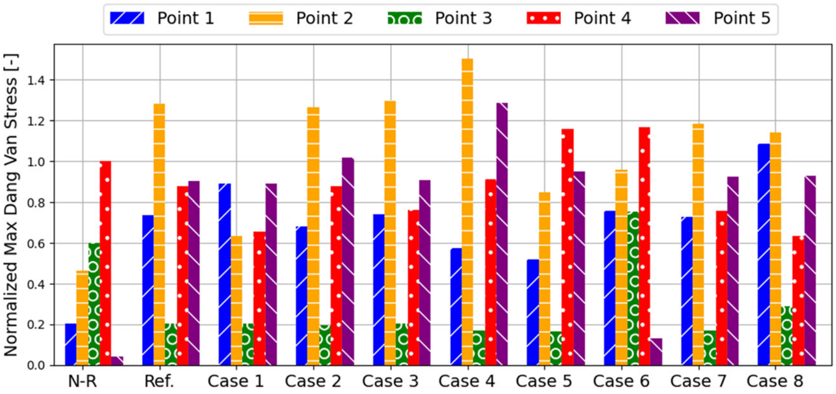

an order of magnitude and are less affected by the over-rollings.

- A rectangular repair cutout geometry induces strong tensile stresses at the rail surface at the start and end stretches of the repaired rail section. This effect is reduced by the chamfered cutout geometry used in field operations today, indicating its effectiveness.
- Shallow repairs induce less overall heat, resulting in faster cooling rates and higher martensite content at the start and end stretches of the repair. Furthermore, as the unfavorable martensite is located closer to the rail surface, there is a risk that the tensile stresses from train wheel over-rollings in this region may cause fatigue cracks. Consequently, shallow repairs are not recommended.
- The slow phase transformations of the filler material ESAB OK Wartrode 3 seem to have a positive effect in preventing the formation of unfavorable material phases.
- The heat input and repair geometry exhibit a complex influence on the material phase fractions, the residual stresses after welding, and the mechanical response under over-rolling. This influence is demonstrated to complicate the crucial task of determining trends for improving the quality of railhead repair welds.

The computational efficiency of the methodology used in this study relies on the simplification to use a 2D model in the mechanical analysis, which may reduce the fidelity of the simulation results. However, given the comparative and qualitative nature of the study, this limitation is not considered to compromise the validity of the presented findings. Another simplification is the omission of heat effects in the modeling of rail surface grinding when removing excess weld material. However, as the impact of this simplification is confined to a shallow depth below the rail surface it is expected to be outweighed by the simulated localized train wheel over-rolling surface loads. Also, the rail surface is typically not the critical region in repaired rail sections. Therefore, despite these limitations, the applied simulation-based assessment is believed to be to of valuable use in other thermo-mechanical-metallurgical processes in railways, e.g., rail surface grinding.

Acknowledgements The current study is part of the ongoing activities in CHARMEC – Chalmers Railway Mechanics (www.chalmers.se/charmec). The numerical simulations were performed on resources provided by Chalmers e-Commons (C3SE). The authors kindly express their gratitude to Professor Jens Nielsen and Professor Johan Ahlström of Chalmers University of Technology for their thoughtful support regarding the over-rolling simulations and experimental work presented in the study. The authors would also like to thank Mr. David Heino and Mr. Anders Hägelmark from the Swedish Transport Administration's Railway Welding School for their valuable help in carrying out the rail head repair welding experiment.

Funding Open access funding provided by Chalmers University of Technology. Through CHARMEC research projects, parts of the study have been funded from the European Union's Horizon 2020 research and innovation programme in the projects In2Track2 and In2Track3 under grant agreements Nos 826255 and 101012456. Funding has also been received from the Horizon Europe research and innovation programme under IAM4RAIL with grant agreement number 101101966.

Data Availability Data is available upon request.

Declarations

Conflict of Interest The authors declare no competing interests.

References

1. Ekberg A (2009) Fatigue of railway wheels. In: Lewis R, Olofsson U (eds) Wheel–rail interface handbook, Woodhead Publishing, pp 211–244. https://doi.org/10.1533/9781845696788.1.211
2. Famurewa SM, Nissen A, Kumar U 2016 Scheduling of railway infrastructure maintenance tasks using train free windows. In: Current trends in reliability, availability, maintainability and safety, Springer International Publishing, Cham, pp 425–436. https://doi.org/10.1007/978-3-319-23597-4_30
3. Ferreira L, Murray MH (1997) Modelling rail track deterioration and maintenance: current practices and future needs. Transp Rev 17(3):207–221. https://doi.org/10.1080/01441649708716982
4. Budai G, Huisman D, Dekker R (2006) Scheduling preventive railway maintenance activities. J Oper Res Soc 57:1035–1044. https://doi.org/10.1057/palgrave.jors.2602085
5. Patel TA, Badheka V (2022) Rail welding technology: processes and welding quality. In: Recent advances in mechanical infrastructure, Springer Nature Singapore, Singapore, pp 369–381. https://doi.org/10.1007/978-981-16-7660-4_33
6. Larsson-Kråik P (2009) Managing the wheel–rail interface: railway infrastructure maintenance in a severe environment: the Swedish experience. In: Lewis R, Olofsson U (eds) Wheel–Rail interface handbook, Woodhead Publishing, pp 633–652. https://doi.org/10.1533/9781845696788.2.634
7. Zhou T (2020) Development of in-suit welding technique to repair rail welded joint with defect. J Mech Civil Eng (IOSR-JMCE) 17(3):44–51. https://doi.org/10.9790/1684-1703024451
8. Dahl B, Mogard B, Gretoft B, Ulander B (1995) Repair of rails on-site by welding. Svetsaren 50:10–14
9. Skyttebol A, Josefson BL (2004) Numerical simulation of flash-butt-welding of railway rail. In: Mathematical modelling of weld phenomena 7, TU Graz Publication, Graz, Austria, p 21

10. Godefroid L, Faria G, Cândido L, Viana T (2015) Failure analysis of recurrent cases of fatigue fracture in flash butt welded rails. Eng Fail Anal 58:407–416. https://doi.org/10.1016/j.engfailanal.2015.05.022
11. Su H, Pun CL, Mutton P, Kan Q, Kang G, Yan W (2021) Numerical study on the ratcheting performance of rail flash butt welds in heavy haul operations. Int J Mech Sci 199:106434. https://doi.org/10.1016/j.ijmecsci.2021.106434
12. Shi X, Liu Y, Liu Z, Hoh HJ, Tsang KS, Pang JHL (2021) An integrated fatigue assessment approach of rail welds using dynamic 3d fe simulation and strain monitoring technique. Eng Fail Anal 120:105080. https://doi.org/10.1016/j.engfailanal.2020.105080
13. Liu Z, Shi X, Tsang K, Hoh H, Pang J (2020) Dynamic finite element modeling and fatigue damage analysis of thermite welds. Fatigue Fract Eng Mater Struct 43(1):119–136. https://doi.org/10.1111/ffe.13091
14. Josefson BL, Bisschop R, Messaadi M, Hantusch J (2020) Residual stresses in thermite welded rails: significance of additional forging. Weld World 64(7):1195–1212. https://doi.org/10.1007/s40194-020-00912-4
15. Arslan MA, Kayabaşı O (2012) 3-d rail–wheel contact analysis using fea. Adv Eng Softw 45(1):325–331. https://doi.org/10.1016/j.advengsoft.2011.10.009
16. Kapoor A, Franklin F, Wong S, Ishida M (2002) Surface roughness and plastic flow in rail wheel contact. Wear 253(1):257–264, S.I. https://doi.org/10.1016/S0043-1648(02)00111-4
17. Brunskill H, Hunter A, Zhou L, Joyce RD, Lewis R (2020) An evaluation of ultrasonic arrays for the static and dynamic measurement of wheel–rail contact pressure and area. Proc IME Part J J Eng Tribol 234(10):1580–1593. https://doi.org/10.1177/1350650120919889
18. Tawfik MN, Padzi MM, Abdullah S, Harmanto D, Firdaws M, Hapaz H (2023) A review of the rolling contact fatigue of rail wheels under various stresses. J Fail Anal Prev 23(1):16–29. https://doi.org/10.1007/s11668-022-01568-6
19. Jiménez S, Barbu L, Oller S, Cornejo A (2022) On the numerical study of fatigue process in rail heads by means of an isotropic damage based high-cycle fatigue constitutive law. Eng Fail Anal 131:105915. https://doi.org/10.1016/j.engfailanal.2021.105915
20. Zhang J, Cai C, Zhu S, Wang M, He Q, Yang S, Zhai W (2022) Experimental investigation on dynamic performance evolution of double-block ballastless track under high-cycle train loads. Eng Struct 254:113872. https://doi.org/10.1016/j.engstruct.2022.113872
21. Tzanakakis K (2013) The railway track and its long term behaviour: a handbook for a railway track of high quality, vol 2. Springer Science & Business Media Verlag Berlin Heidelberg. https://doi.org/10.1007/978-3-642-36051-0
22. Lidén T (2018) Concurrent planning of railway maintenance windows and train services, vol 1957. Linköping University Electronic Press. https://doi.org/10.3384/diss.diva-152491
23. Al-Douri YK, Tretten P, Karim R (2016) Improvement of railway performance: a study of Swedish railway infrastructure. J Modern Transp 24(1):22–37. https://doi.org/10.1007/s40534-015-0092-0
24. Lindgren LE (2001) Finite element modeling and simulation of welding. Part 1: increased complexity. J Therm Stress 24(2):141–192. https://doi.org/10.1080/01495730150500442
25. Lindgren LE (2001) Finite element modeling and simulation of welding. Part 2: improved material modeling. J Therm Stress 24:195–231. https://doi.org/10.1080/014957301300006380
26. Lindgren LE (2001) Finite element modeling and simulation of welding. Part 3: efficiency and integration. J Therm Stress 24(4):305–334. https://doi.org/10.1080/01495730151078117
27. Ma N, Cai Z, Huang H, Deng D, Murakawa H, Pan J (2015) Investigation of welding residual stress in flash-butt joint of u71mn rail steel by numerical simulation and experiment. Mater Des 88:1296–1309. https://doi.org/10.1016/j.matdes.2015.08.124
28. Chen Y, Lawrence FV, Barkan CPL, Dantzig JA (2006) Heat transfer modelling of rail thermite welding. Proc IME Part F J Rail Rapid Transit 220(3):207–217. https://doi.org/10.1243/09544097F01505
29. Cal Z, Nawafune M, Ma N, Qu Y, Cao B, Murakawa H (2011) Residual stresses in flash butt welded rail. Trans JWRI 40(1):79–87. https://doi.org/10.18910/4606
30. Fang XY, Zhang HN, Ma D-W, Wu ZJ, Huang W (2022) Influence of welding residual stress on subsurface fatigue crack propagation of rail. Eng Fract Mech 271:108642. https://doi.org/10.1016/j.engfracmech.2022.108642
31. Lu C, Nieto J, Puy I, Melendez J, Martínez-Esnaola J (2018) Fatigue prediction of rail welded joints. Int J Fatigue 113:78–87. https://doi.org/10.1016/j.ijfatigue.2018.03.038
32. Wu Y, Pun CL, Su H, Huang P, Welsby D, Mutton P, Yan W (2022) Numerical study on ratcheting performance of heavy haul rail flash-butt welds in curved tracks. Eng Fail Anal 140:106611. https://doi.org/10.1016/j.engfailanal.2022.106611
33. Gedney BL, Rizos DC (2022) Combining welding-induced residual stress with thermal and mechanical stress in continuous welded rail. Res Eng 16:100777. https://doi.org/10.1016/j.rineng.2022.100777
34. Wang YQ, Zhou H, Shi YJ, Feng BR (2012) Mechanical properties and fracture toughness of rail steels and thermite welds at low temperature. Int J Miner Metall Mater 19(5):409–420. https://doi.org/10.1007/s12613-012-0572-8
35. Zerbst U, Mädler K, Hintze H (2005) Fracture mechanics in railway applications—an overview. Eng Fract Mech 72(2):163–194. https://doi.org/10.1016/j.engfracmech.2003.11.010
36. Cannon DF, Edel K-O, Grassie SL, Sawley K (2003) Rail defects: an overview. Fatigue Fract Eng Mater Struct 26(10):865–886. https://doi.org/10.1046/j.1460-2695.2003.00693.x
37. Esmaeili A, Ahlström J, Andersson B, Ekh M (2021) Modelling of cyclic plasticity and phase transformations during repeated local heating events in rail and wheel steels. Int J Fatigue 151:106361. https://doi.org/10.1016/j.ijfatigue.2021.106361
38. Andersson B, Ahlström J, Ekh M, Josefson BL (2022) Homogenization based macroscopic model of phase transformations and cyclic plasticity in pearlitic steel. J Therm Stress 45(6):470–492. https://doi.org/10.1080/01495739.2022.2056557
39. Andersson B, Ekh M, Josefson BL (2024) Computationally efficient simulation methodology for railway repair welding: cyclic plasticity, phase transformations and multi-phase homogenization. J Therm Stress 47(2):164–188. https://doi.org/10.1080/01495739.2023.2283309
40. Jaiswal J, Smith SF, Cox R, Kabo E (2018) Repair of discrete rail head defects – a novel technology. In: Collection of open conferences in research transport, Zenodo. https://doi.org/10.5281/zenodo.1473576
41. Kabo E, Ekberg A, Maglio M (2019) Rolling contact fatigue assessment of repair rail welds. Wear 436–437:203030. https://doi.org/10.1016/j.wear.2019.203030
42. Jun HK, Kim DW, Jeon IS, Lee SH, Chang YS (2017) Investigation of residual stresses in a repair-welded rail head considering solid-state phase transformation. Fatigue Fract Eng Mater Struct 40(7):1059–1071. https://doi.org/10.1111/ffe.12564
43. Banöverbyggnad (2022) svetsning, bearbetning och smörjning, Tech. Rep. TRVINFRA-00016, Trafikverkets infrastrukturregelverk, Borlänge, Sweden
44. Svetsning av räler och rälskomponenter (2018) svetsarprövning, Tech. Rep. TDOK 2014:0587, Trafikverkets infrastrukturregelverk, Borlänge, Sweden

45. Svetsning av räler och rälskomponenter (2018) godkännande av svetsprocedurer, Tech. Rep. TDOK 2014:0586, Trafikverkets infrastrukturregelverk, Borlänge, Sweden
46. Railway applications (2009) Track - restoration of rails by electric arc welding. EN 15594:2009(E), European Committee for Standardization (CEN), Brussels
47. ESAB (2023) Ok weartrode 30. https://esab.com/no/eur_sv/products-solutions/product/filler-metals/hardfacing/stick-electrodes-smaw/ok-weartrode-30/
48. Welding consumables (2022) Welding consumables for hardfacing. BS EN 14700:2022, European Committee for Standardization (CEN), Brussels
49. Banöverbyggnad - oförstörande provning (2020) Tech. Rep. TRVINFRA-00015, Trafikverkets infrastrukturregelverk, Borlänge, Sweden
50. Railway applications (2011) Track. Rail. Vignole railway rails 46 kg/m and above, BS EN 13674-1:2011+A1:2017, European Committee for Standardization (CEN), Brussels
51. Denis S, Farias D, Simon A (1992) Mathematical model coupling phase transformations and temperature evolutions in steels. ISIJ Int 32(3):316–325. https://doi.org/10.2355/isijinternational.32.316
52. Fernandes FMB, Denis S, Simon A (1985) Mathematical model coupling phase transformation and temperature evolution during quenching of steels. Mater Sci Technol 1(10):838–844. https://doi.org/10.1179/mst.1985.1.10.838
53. Scheil E (1935) Anlaufzeit der austenitumwandlung. Archiv für das Eisenhüttenwesen 8(12):565–567. https://doi.org/10.1002/srin.193500186
54. Verdi C, Visintin A (1987) A mathematical model of the austenite-pearlite transformation in plain carbon steel based on the scheil's additivity rule. Acta Metall 35(11):2711 – 2717. https://doi.org/10.1016/0001-6160(87)90270-7
55. Koistinen D, Marburger R (1959) A general equation prescribing the extent of the austenite-martensite transformation in pure iron-carbon alloys and plain carbon steels. Acta Metall 7(1):59 – 60. https://doi.org/10.1016/0001-6160(59)90170-1
56. Sente-Software (2018) Jmatpro 6.0. https://www.sentesoftware.co.uk/jmatpro
57. Hutchinson J (1970) Elastic-plastic behaviour of polycrystalline metals and composites. Proc R Soc A Math Phys Eng Sci 319:247–272. https://doi.org/10.1098/rspa.1983.0054
58. Lebensohn RA, Turner PA, Signorelli JW, Canova GR (1998) Calculation of intergranular stresses based on a large-strain viscoplastic self-consistent polycrystal model. Model Simul Mater Sci Eng 6:447–465. https://doi.org/10.1088/0965-0393/6/4/011
59. Lebensohn RA, Tomé CN, Castañeda PP (2007) Self-consistent modelling of the mechanical behaviour of viscoplastic polycrystals incorporating intragranular field fluctuations. Phil Mag 87(28):4287–4322. https://doi.org/10.1080/14786430701432619
60. Chaboche J (1989) Constitutive equations for cyclic plasticity and cyclic viscoplasticity. Int J Plast 5(3):247 – 302. https://doi.org/10.1016/0749-6419(89)90015-6
61. Greenwood GW, Johnson R (1965) The deformation of metals under small stresses during phase transformations. Proc R Soc Lond Ser A Math Phys Sci 283(1394):403–422. https://doi.org/10.1098/rspa.1965.0029
62. Magee CL (1966) Transformation kinetics, microplasticity and aging of martensite in Fe-31Ni, Ph.D. thesis, Carnegie Institute of Technology, Pittsburgh, Pa
63. Wolff M, Böhm M, Suhr B (2009) Comparison of different approaches to transformation-induced plasticity in steel. Materialwissenschaft und Werkstofftechnik: Entwicklung, Fertigung, Prüfung, Eigenschaften und Anwendungen technischer Werkstoffe 40(5–6):454–459. https://doi.org/10.1002/mawe.200900476
64. Leblond J, Mottet G, Devaux J (1986) A theoretical and numerical approach to the plastic behaviour of steels during phase transformations—II. Study of classical plasticity for ideal-plastic phases. J Mech Phys Solids 34(4):411–432. https://doi.org/10.1016/0022-5096(86)90010-4
65. Fischer F, Reisner G, Werner E, Tanaka K, Cailletaud G, Antretter T (2000) A new view on transformation induced plasticity (trip). Int J Plast 16(7):723–748. https://doi.org/10.1016/S0749-6419(99)00078-9
66. Dong P (2018) On repair weld residual stresses and significance to structural integrity. Weld World 62(2):351–362. https://doi.org/10.1007/s40194-018-0554-1
67. Goldak J, Chakravarti A, Bibby M (1984) A new finite element model for welding heat sources. Metall Trans B 15:299–305. https://doi.org/10.1007/BF02667333
68. Goldak J, Bibby M, Moore J, House R, Patel B (1986) Computer modeling of heat flow in welds. Metall Trans B 17(3):587–600. https://doi.org/10.1007/BF02670226
69. Abaqus analysis user's manual (2018) 2018th edn, Dassault Systèmes Simulia Corp, Providence, Rhode Island USA
70. Lindgren LE, Runnemalm H, Näsström MO (1999) Simulation of multipass welding of a thick plate. Int J Numer Methods Eng 44(9):1301–1316. https://doi.org/10.1002/(SICI)1097-0207(19990330)44:9<1301::AID-NME479>3.0.CO;2-K
71. Mughal MP, Fawad H, Mufti RA, Siddique M (2005) Deformation modelling in layered manufacturing of metallic parts using gas metal arc welding: effect of process parameters. Model Simul Mater Sci Eng 13(7):1187. https://doi.org/10.1088/0965-0393/13/7/013
72. Abid M, Siddique M (2005) Numerical simulation to study the effect of tack welds and root gap on welding deformations and residual stresses of a pipe-flange joint. Int J Press Vessel Pip 82(11):860–871. https://doi.org/10.1016/j.ijpvp.2005.06.008
73. Andersson B (2024) Thermo-mechanical-metallurgical modelling of pearlitic steels and railhead repair welding, Ph.D. thesis, Chalmers University of Technology
74. Skrypnyk R, Ekh M, Nielsen J, Pålsson B (2019) Prediction of plastic deformation and wear in railway crossings – comparing the performance of two rail steel grades. Wear 428–429. https://doi.org/10.1016/j.wear.2019.03.019
75. Skrypnyk R, Nielsen JC, Ekh M, Pålsson BA (2019) Metamodelling of wheel–rail normal contact in railway crossings with elasto-plastic material behaviour. Engineering with Computers 35(1):139–155. https://doi.org/10.1007/s00366-018-0589-3
76. Ansin C, Pålsson B, Ekh M, Larsson F, Larsson R (2022) Simulation and field measurements of the long-term rail surface damage due to plasticity, wear and surface rolling contact fatigue cracks in a curve. Proceedings of the 12th international conference on contact mechanics and wear of rail/wheel systems 591–601
77. Dang Van K, Cailletaud G, Flavenot JF, Le Douaron A, Lieurade HP (1989) Criterion for high cycle fatigue under multiaxial loading, Biaxial and Multiaxial Fatigue, EGF 3, Mechanical Engineering Publications, London, pp 459–478
78. Josefson BL, Ringsberg JW (2009) Assessment of uncertainties in life prediction of fatigue crack initiation and propagation in welded rails. Int J Fatigue 31(8):1413–1421. https://doi.org/10.1016/j.ijfatigue.2009.03.024
79. Salehi I, Kapoor A, Mutton P (2011) Multi-axial fatigue analysis of aluminothermic rail welds under high axle load conditions. Int J Fatigue 33(9):1324–1336. https://doi.org/10.1016/j.ijfatigue.2011.04.010
80. Gery D, Long H, Maropoulos P (2005) Effects of welding speed, energy input and heat source distribution on temperature variations in butt joint welding. J Mater Process Technol 167(2):393–401. 2005 International Forum on the Advances in Materials Processing Technology. https://doi.org/10.1016/j.jmatprotec.2005.06.018

81. Long H, Gery D, Carlier A, Maropoulos P (2009) Prediction of welding distortion in butt joint of thin plates. Mater Des 30(10):4126–4135. https://doi.org/10.1016/j.matdes.2009.05.004
82. Deng D, Zhou Y, Bi T, Liu X (2013) Experimental and numerical investigations of welding distortion induced by co2 gas arc welding in thin-plate bead-on joints. Mater Des 1980–2015(52):720–729. https://doi.org/10.1016/j.matdes.2013.06.013
83. Suwanpinij P, Thonondaeng T, Kumma P, Suksawat B, Lothongkum G (2022) Control of the bainitic structure for a wear-resisting hard-faced rail track. Materials Testing 64(1):1–10. https://doi.org/10.1515/mt-2021-2076
84. Moran SP, Erbe DJ, Herwig WE, Hoffman WE, Hsu C, Reynolds J (2004) "Arc welding power sources" in welding handbook, Part 1: Welding Processes, vol 2, 9th edn. American Welding Society, Miami, Florida, USA
85. Popovic O, Prokic-Cvetkovic R (2012) Surface welding as a way of railway maintenance. In: Mechanical engineering, IntechOpen, pp 233–253. https://doi.org/10.5772/35403
86. Kallander S (2023) Rail maintinance specialist, the Swedish transport administration, Personal communication, regarding confidential rail fracture reports
87. Ringsberg JW, Skyttebol A, Josefson BL (2005) Investigation of the rolling contact fatigue resistance of laser cladded twin-disc specimens: Fe simulation of laser cladding, grinding and a twin-disc test. Int J Fatigue 27(6):702–714. https://doi.org/10.1016/j.ijfatigue.2004.10.006
88. Lewis S, Lewis R, Fletcher D (2015) Assessment of laser cladding as an option for repairing/enhancing rails. Wear 330-331:581–591. https://doi.org/10.1016/j.wear.2015.02.027
89. Meng L, Zhao W, Hou K, Kou D, Yuan Z, Zhang X, Xu J, Hu Q, Wang D, Zeng X (2019) A comparison of microstructure and mechanical properties of laser cladding and laser-induction hybrid cladding coatings on full-scale rail. Mater Sci Eng A 748:1–15. https://doi.org/10.1016/j.msea.2019.01.068